Nanosecond-Timescale Conformational Dynamics of the Human α7 Nicotinic Acetylcholine Receptor

Xiaolin Cheng,* Ivaylo Ivanov,*† Hailong Wang,‡ Steven M. Sine,‡ and J. Andrew McCammon*†
*Howard Hughes Medical Institute, National Science Foundation Center for Theoretical Biophysics, Department of Chemistry and Biochemistry, and †Department of Pharmacology, University of California, San Diego, La Jolla, California; and ‡Receptor Biology Laboratory, Department of Physiology and Biomedical Engineering, Mayo Clinic College of Medicine, Rochester, Minnesota

ABSTRACT We explore the conformational dynamics of a homology model of the human α7 nicotinic acetylcholine receptor using molecular dynamics simulation and analyses of root mean-square fluctuations, block partitioning of segmental motion, and principal component analysis. The results reveal flexible regions and concerted global motions of the subunits encompassing extracellular and transmembrane domains of the subunits. The most relevant motions comprise a bending, hinged at the β10-M1 region, accompanied by concerted tilting of the M2 helices that widens the intracellular end of the channel. Despite the nanosecond timescale, the observations suggest that tilting of the M2 helices may initiate opening of the pore. The results also reveal direct coupling between a twisting motion of the extracellular domain and dynamic changes of M2. Covariance analysis of interresidue motions shows that this coupling arises through a network of residues within the Cys and M2-M3 loops where Phe^{135} is stabilized within a hydrophobic pocket formed by Leu^{270} and Ile^{271}. The resulting concerted motion causes a downward shift of the M2 helices that disrupts a hydrophobic girdle formed by 9′ and 13′ residues.

INTRODUCTION

Fast synaptic transmission depends on postsynaptic receptors to detect nerve-released transmitter molecules and subsequently change the membrane potential of the receiving cell. Postsynaptic receptors of the Cys-loop superfamily are found throughout the nervous system, where they mediate either excitation or inhibition. Each receptor in the superfamily contains five pseudosymmetric subunits, each containing a signature sequence of 13 residues bordered by cysteines that form a disulfide-bonded loop at the junction of extracellular and pore domains. Fundamental steps in receptor activation include neurotransmitter recognition, coupling of recognition to opening of the ion pore, and passive flow of ions through the pore (1). Insight into these fundamental steps advanced recently due to structural determinations that defined the overall atomic architecture and allowed construction of atomic-scale models. However, our understanding of structural motions underlying receptor activation is just beginning to develop.

Both experimental and computational approaches have probed structural motions underlying Cys-loop receptor function, and have focused on three main structural domains. Motions in the binding domain have been inferred from x-ray structures of apo and agonist-bound forms of acetylcholine binding protein (AChBP), and suggest that a hairpin structure known as the C-loop traps the agonist within the aromatic-rich binding pocket (2,3). A trapping motion of the C-loop was also suggested by agonist-dependent changes in accessibility of intrinsic tryptophans to a fluorescence quencher (4), hydrogen-deuterium exchange (5), and chemical shift by NMR (6). Molecular dynamics (MD) simulations of AChBP or of models of the homopentameric α7 nicotinic acetylcholine receptor (nAChR) show that without agonist bound, the C-loop is highly flexible, but that with agonist bound it becomes restricted in the trapping conformation (4,7).

The junction of the neurotransmitter binding and pore domains is structurally well situated to couple agonist binding to gating of the pore. Its role in coupling has been assessed from changes in solvent accessibility of cysteine-substituted residues (8,9) and functional consequences of disulfide trapping (10,11). Within the core of the binding-pore junction, conserved Arg and Glu residues form a crucial functional link between binding and gating domains (12), and targeted MD simulations of a model of the α7 receptor suggest that the salt bridge stabilizes further when the C-loop changes from open to trapping conformations (13). Additional structural elements in the binding-pore junction also contribute to the coupling process, including the Cys, β1-β2, and β8-β9 loops from the binding domain, and the M2-M3 loop from the pore domain (14).

Structural changes in the pore were inferred from cryoelectron microscopy (cryo-EM) of the *Torpedo* receptor with and without bound ACh, and suggested a rotation of the five pore-lining α-helices, causing collapse of a central hydrophobic girdle (15). However, subsequent studies have yielded a mixed picture. A simple dilation mechanism was suggested by assessment of residues that line the pore in the open state by measuring the ability of protons to block the channel after lysine substitution (16), whereas placement of Zn^{2+} binding sites at various levels in the pore suggested a tilting of the M2 helices (17).

Submitted March 29, 2007, and accepted for publication June 8, 2007.

Address reprint requests to Xiaolin Cheng, Dept. of Chemistry and Biochemistry, University of California, San Diego, 9500 Gilman Dr., La Jolla, CA 92093. Tel.: 858-822-0169; Fax: 858-534-4974; E-mail: xcheng@mccammon.ucsd.edu.

Editor: Jose Onuchic.

0006-3495/07/10/2622/13 $2.00

doi: 10.1529/biophysj.107.109843

Insights into global motions underlying gating have emerged from rate-equilibrium free-energy relationship (REFER) analyses of the gating transition state, which suggest a cascadelike conformational change from the binding site to the pore (18). Normal-mode analysis probing the intrinsic flexibility of the receptor suggested that an inherent quaternary twisting motion may accompany gating (19,20). Dynamics studies of a model of the α7 ligand-binding domain revealed asymmetrical positioning of the subunits in the apo and antagonist bound states, but showed symmetrical positioning with agonist bound (21,22).

Up to now, only one MD simulation has been performed on the nAChR containing both ligand-binding and transmembrane domains (7). In that simulation, the receptor showed a twist-to-close motion in which movements of the C-loop correlated with a 10° rotation and inward movement of two nonadjacent subunits. However, because a full receptor structure was not available at that time, the simulation started from a chimeric model based on coordinates from AChBP (23) and the transmembrane domain from the *Torpedo* nAChR (24). Here, we carry out MD simulation on a new homology model of α7 based on the cryo-EM structure of the *Torpedo* nAChR. The resulting model differs substantially from the previous one, particularly at the interface dividing binding and pore domains (20), and the concerted global motions that emerge also differ from those previously suggested (7). The results also reveal dynamic coupling between the signature Cys-loop and the M2-M3 linker that may contribute to gating of the channel.

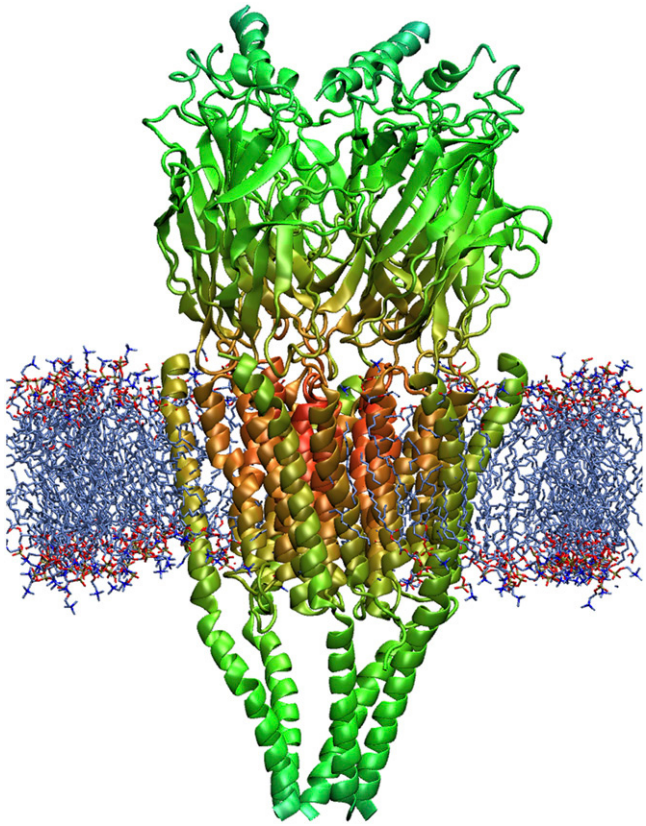

FIGURE 1 Snapshot of the simulation system with the human α7 receptor (*ribbon*) inserted into the POPC lipid bilayer (*licorice*) and fully hydrated with water molecules (not shown).

METHODS

Homology modeling

The homology model of the human α7 acetylcholine receptor was constructed with Modeller v8.0 (25,26) based on the 4.0-Å resolution cryo-EM structure of *Torpedo* nAChR (PDB code 2BG9). Details of the modeling procedure were described previously (20). Briefly, the modeled structure contained 1835 residues comprising the ligand-binding and transmembrane domains, as well as part of the cytoplasmic vestibule that spans M3 and M4. Fivefold symmetry was not imposed when modeling the pentameric structure. In the final model, the C-loops in two alternating subunits (A and D subunits) had the open conformation, as observed for the two α-subunits of the *Torpedo* structure, whereas the remaining three subunits (B, C, and E) showed the more contracted C-loop conformation based on the β, δ, and γ subunits. The final models were evaluated with PROCHECK (27) and Prosa 2003 (28).

MD simulations

MD simulation was performed with the nAChR model embedded in a fully hydrated, 120 × 120-Å palmitoyl-2-oleoyl-*sn*-glycerol-phosphatidylcholine (POPC) bilayer (Fig. 1). This resulted in a total of ~290 POPC molecules and ~60600 water molecules. Charge neutralization was accomplished with the addition of 86 Na^+ and 26 Cl^- ions, resulting in a 0.1 M solution. The solvated system then underwent four equilibration steps: 1), 2000 steps of energy minimization with a fixed protein backbone; 2), five cycles of a 500-step minimization with decreasing positional restraints on the protein C^α atoms; 3), gradual temperature increase from 50 K to 310 K in 10,000 steps of constant-volume MD (NVT ensemble) simulation with harmonic restraints (with force constant of 3 kcal·mol^{-1}·Å^{-2}) on the protein C^α atoms; and 4), 2 ns constant surface-area ensemble MD equilibration with decreasing positional restraints on the C^α atoms. Here, extensive equilibration procedures have been used to relax the system due to the relatively low resolution of the starting structure. Also, particular attention was paid to the packing of the lipids, which make direct contact with M4 and are therefore expected to affect the overall structure and dynamics of the transmembrane domain. We carefully monitored the equilibration of both the protein and the lipid bilayer, and have gained confidence that the artifacts due to the initial model and/or setup have been minimized within the limits of the structural data available.

The MD simulation was performed with the NAMD2 program (29) and the CHARMM27 force field (30). A short-range cutoff of 9 Å was used for nonbonded interactions, and long-range electrostatic interactions were treated with a particle mesh Ewald method (31). Langevin dynamics and a Langevin piston algorithm were used to maintain the temperature at 310 K and a pressure of 1 atm. The r-RESPA multiple-time-step method was employed, with time steps of 2 fs for bonded, 2 fs short-range for nonbonded, and 4 fs for long-range electrostatic forces. The bonds between hydrogen and heavy atoms were constrained with the SHAKE algorithm. All simulations were conducted on DataStar, an IBM terascale machine at the San Diego Supercomputer Center.

Data analysis

Principal component analysis (PCA) is a technique that transforms a number of (possibly) correlated variables into a (smaller) number of uncorrelated

variables called principal components while retaining those characteristics of the data set that contribute most to its variance. This method is based on the analysis of the covariance matrix $\mathbf{\Gamma}$ obtained from the MD trajectory data. The elements of the covariance matrix $\mathbf{\Gamma}$ are defined as

$$\Gamma_{ij} = \langle (x_i(t) - \langle x_i(t) \rangle) \times (x_j(t) - \langle x_j(t) \rangle) \rangle, \quad (1)$$

where $x_i(t)$ and $x_j(t)$ are the Cartesian coordinates for atoms i and j, respectively, at time t. The angle brackets denote the time average over the entire trajectory. Diagonalization of the covariance matrix $\mathbf{\Gamma}$ yields the set of eigenvectors $\{\nu_i\}$ called principal components and associated eigenvalues $\{\lambda_i\}$. Each eigenvalue λ_i represents the mean-square fluctuations along the principal component ν_i. From the root mean-square fluctuations it is possible to define effective frequencies ω_i^{eff} for the principal components as follows:

$$\omega_i^{\text{eff}} = \sqrt{\frac{k_B T}{\lambda_i}}. \quad (2)$$

In the case of a harmonic energy surface, results from normal-mode analysis and PCA are identical provided that the root mean-square fluctuations are converged. For an anharmonic energy surface, the extent to which the principal modes resemble normal modes is dependent on how readily the surface can be represented by a harmonic approximation.

In our calculation, PCA was performed on the C^α atoms of individual subunits using the GROMACS suite of programs (32). The entire 10-ns trajectory is used in PCA. Before the analysis, each frame is superimposed to the first frame to remove the rotational and translational degrees of freedom. The eigenvectors $\{\nu_i\}$ were ordered according to magnitude of the root mean-square fluctuation $\{\lambda_i\}$(or the respective effective frequency ω_i^{eff}).

The TLS (Translation/Libration/Screw) formalism was originally developed to predict thermal parameters of small molecules subjected to x-ray crystallography, but it was later successfully extended to describing rigid-body motion of large groups of atoms in proteins, such as flexible-loop and domain motions. We have used the TLSMD web server (33) (http://skuld.bmsc.washington.edu/~tlsmd/) for our rigid-body motion analysis. In this treatment, the optimal multigroup TLS partition along a protein chain is obtained by optimizing the thermal parameters predicted by the trial TLS models against the input ones (i.e., as observed in a crystallographic electron-density map or MD trajectory data). Diffraction or simulation studies yield information not only about mean atomic positions but also about the probability density functions of atomic displacement from these mean positions. The thermal parameters, including isotropic or anisotropic atomic displacement parameters, are defined as the mean-square displacements using Gaussian approximations of the probability density functions. The TLSMD program first generates all possible partitions up to a specified maximum number of TLS segments. For each of these segments, its rigid-body displacement parameters (TLS model) are optimized such that they best reproduce the input thermal parameters of the atoms contained in this segment. Then the residual between the predicted (based on the derived TLS model) and the input thermal parameters is computed. The residuals from all the segments are added together to give the sum of residuals for any given partition. After exhausting every possible sequence of continuous TLS segments for the chain, the partition with the lowest residual sum is chosen as the optimal TLS model. In our analysis, the input thermal parameters are the atomic displacement parameters calculated from the MD trajectory data using the GROMACS program.

Cross-correlation analysis was applied to correlate motions between any pair of residues in the $\alpha 7$ receptor model. The cross-correlation coefficient C_{ij}, between atoms i and j, is a measure of the correlated nature of their atomic fluctuations and is computed as follows:

$$C_{ij} = \langle \Delta r_i \times \Delta r_j \rangle / (\langle \Delta r_i \times \Delta r_i \rangle \langle \Delta r_j \times \Delta r_j \rangle)^{1/2}, \quad (3)$$

where Δr_i and Δr_j are the displacement vectors for atoms i and j, respectively. The angle brackets denote an average over the trajectory. The value of C_{ij} ranges from -1 to 1 with the correlated (positive) residue pair moving in the same direction, and the anticorrelated (negative) pair moving in the opposite direction. The extent of correlation between motions of C^α atoms was calculated using the GROMACS program.

Pore-radius profiles were determined with the HOLE (34) program. Both lateral and radial tilting angles were calculated for all five M2 helices. Using a rigid-body fitting procedure, the lateral tilting angle was defined as the angle between the principal axis of M2 and the membrane normal (and in the local tangent plane to the cylinder wall of the five M2 helices (see Fig. 8 *a*)), and the radial tilting angle was defined as the angle perpendicular to the cylinder wall (see Fig. 8 *b*). All figures were prepared with the program VMD (35).

RESULTS

Root mean-square fluctuation

The root mean-square deviation relative to the starting structure gradually levels off after the initial 2–3 ns (Supplementary Material, Fig. S1), indicating that the homology model provides a reasonable starting structure for the simulation. Fig. 2 *a* illustrates the root mean-square fluctuations (RMSFs) of the C^α atoms from the current simulation (*black line*), along with the results from previous MD simulation (7) (*red line*) and normal-mode analysis (*green line*) (20). Considerable similarity is observed for both MD simulations, which confirms that the intrinsic flexibility of the protein is not sensitive to its precise structure. Compared with the two MD simulations, the normal-mode result shows some major differences. This is not surprising, given that the normal-mode analysis employs a simple representation of system, lacking explicit solvent, ions, and the bilayer, and may thus be biased for certain regions (e.g., the exaggerated motion in M4, less mobility in $\beta 8$-$\beta 9$).

The computed B-factor values are color-coded onto the three-dimensional structure of one subunit for easy visualization (Fig. 2 *b*). Clearly, most secondary structural elements, such as the β-strands in the extracelluar domain, exhibit low flexibility. A region that fluctuates most significantly is the C-loop, which is found to move away from the binding pocket in all five subunits except in the E subunit. This result is consistent with those pf previous experimental (4) and computational (21) studies, which indicate that the C-loop is flexible when the ligand is not present. Another region that displays significant flexibility is the $\beta 8$-$\beta 9$ loop, consistent with disorder of this region in the cryo-EM structure (36). Other mobile regions within the extracellular domain include the Cys-loop, the $\beta 1$-$\beta 2$ linker, the $\beta 5$-$\beta 5'$ loop and the N-terminus. Both the conserved Cys-loop and the $\beta 1$-$\beta 2$ linker are essential for channel gating of the nAChR (37,38), and their movements are thus expected to play a role in coupling ligand binding to channel gating.

In the transmembrane domain, considerable mobility is seen for two regions. One is the M2-M3 linker and the other is the C-terminus of M3. The mobility of the M2-M3 linker is consistent with earlier experimental findings that residues on the M2-M3 linker change their contacting environments during the transition from the resting to the open state (39,40), suggesting that it undergoes some conformational change. It is of import that the observed motion of the M2-M3 linker

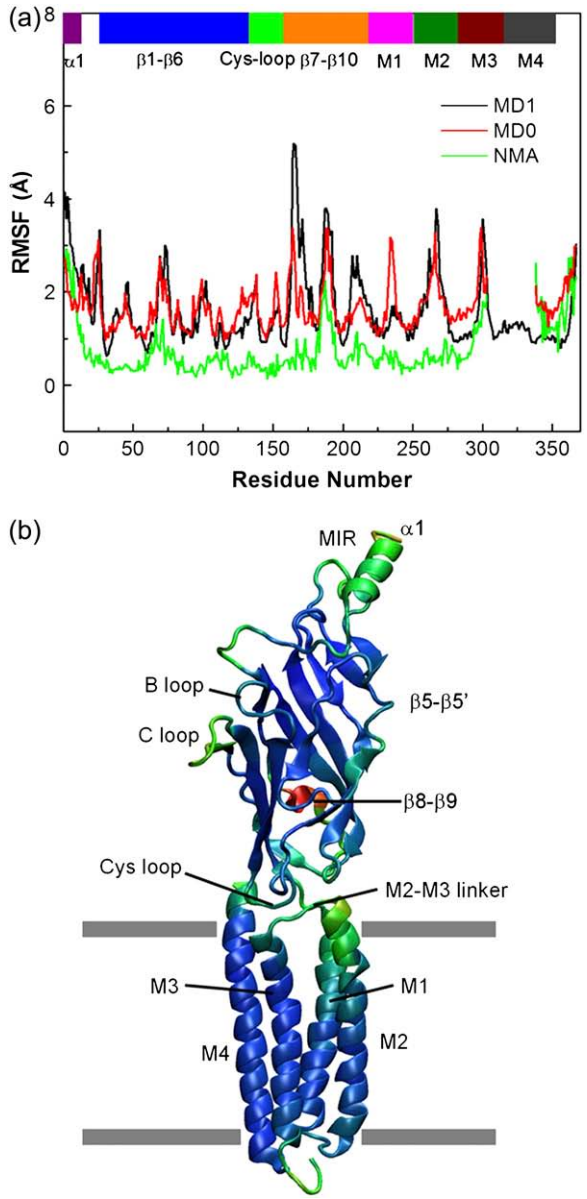

FIGURE 2 (*a*) RMSFs of the C^{α} atoms from the MD simulation presented here (*black line*) along with those from a previous MD simulation (*red line*) and from the block normal mode analysis (*green line*). The color bar on the top of Fig. 2 *a* indicates sequence position of important structural elements; these structural elements are also labeled in Fig. 2 *b*. (*b*) The computed B-factor values are color-coded onto a single subunit of the receptor, with red corresponding to the most mobile region and blue corresponding to the most stable region. For clarity, the RMSFs are averaged over five subunits.

allows an atomic description of the coupling between the movements of the ligand-binding and transmembrane domains, which will be analyzed below in more detail. The considerable fluctuation seen in the C-terminus of M3 is expected, given that part of the intracellular loop connected to it is not present in the simulation. Only small movements are noted in the M4 helix (residues 304–367), which differs somewhat from previous computational studies (7,19,20). The absence of motion in M4 is, however, closer to the conclusion that the entire M4 segment moves as a rigid body, as suggested by ϕ-value analysis of this segment (41).

Concerted motions within individual subunits

Channel gating has been envisioned as a quasiharmonic, low-frequency motion that occurs within an individual energy basin (19,20,42). We found PCA to be a versatile tool for analyzing protein dynamics in terms of low-frequency motions, and useful in confirming observations made during visual inspection of the trajectory. As PCA reduces the dimensionality of the trajectory data, it highlights important dynamical features with the first few principal modes describing collective, global motions of the system occurring within the 10-ns simulation time. Since motion within a single subunit is more correlated than that between adjacent subunits, our PCA analysis focuses on the C^{α} atoms for one of the subunits.

The majority of motions in the MD trajectory are captured by the first three PCA modes. In fact, the first three eigenvalues account for ~50% of the overall fluctuations. Motion in the first PCA mode involves a bending hinged at the junction of β10 and M1 (Fig. 3 *a*; an animated image is provided in Supplementary Material, Fig. S2). Coupled with a twisting motion of the distal end of the ligand-binding domain (the α1 helix and MIR region), the Cys- and β1-β2 loops rotate slightly toward each other, and simultaneously move away from the membrane surface. The C-loop undergoes a swing type of motion that extends to the β10-M1 region. Both the M2 and M3 helices undergo significant tilting motions, accompanied by a downward shift of the M2-M3 linker. The tilting motion of M2 sharply contrasts with the concerted rotation proposed (24) and observed (7) previously, and will be further analyzed in the section titled Dynamics of the transmembrane helices.

Motion in the second mode involves an expansion localized to the middle of the ligand-binding domain involving the A- and C-loops on one side of the subunit and the β8-β9 loop on the other side (Fig. 3 *b*; an animated image is provided in Supplementary Material, Fig. S3). These three loops sit at the interface between subunits and contribute to the ligand-binding sites. The concerted motion of these loops may thus be important in the mechanism of ligand binding, in agreement with experimental results showing large changes in gating upon perturbation of these regions (18,43–45). The second PCA mode shows little motion in the transmembrane domains, indicating that the extracellular and transmembrane domains are less coupled in this mode.

A twisting motion of the M2-M3 linker is most apparent in the third PCA mode (Fig. 3 *c*; an animated image is provided in Supplementary Material, Fig. S4), in agreement with previous simulations (7) and the contributions to channel gating demonstrated by site-directed mutagenesis of the M2-M3 linker (9,11,46). Also present are motions of the C-loop

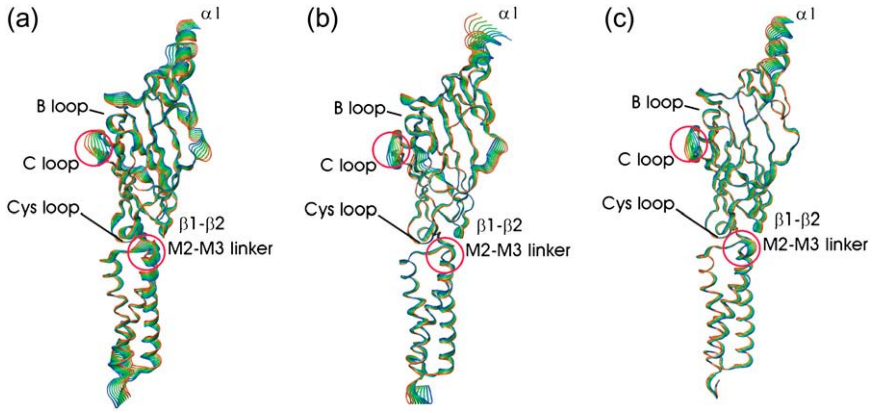

FIGURE 3 Global motions of the α7 receptor during the simulation, as suggested by the PCA analysis. The model structures are generated from some small displacements along (*a*) the first, (*b*) the second, and (*c*) the third principal modes. Some key regions are highlighted with red circles.

and α1 helix, although with much smaller magnitude compared to the first two modes.

TLS analysis (motion in blocks)

REFER experiments reveal that sequential structural changes in a few discrete domains, called blocks, contribute to the transition state leading to gating of the pore (41,47). Each gating block is defined as a contiguous structural element in which all residues show the same ϕ-value after structural perturbation, and thus appear to move as a rigid body. The concept of ''block'' not only provides insight into the nature of gating dynamics, but also justifies the development of less computationally intensive, coarse-grained models to simulate channel gating.

To extract dynamical block information from the MD trajectory, we use a procedure called TLSMD (translation/libration/screw motion determination) to identify the moving blocks based on anisotropic atomic displacement parameters derived from the simulation (33,48). The basic idea underlying the TLSMD algorithm is that if any two atoms belong to the same rigid-body group, then the atomic displacement parameters for these two atoms should have the same displacement probability. The algorithm, which recursively partitions the protein structure into a number of domains, is hierarchical in nature. The partition starts with two blocks and then introduces more blocks to achieve progressively better fitting of the atomic displacement parameters.

Partitioning the ligand binding domain into two blocks reproduces the thermal parameters reasonably well and positions the block boundary near the C-terminus of the Cys-loop. Previously, by comparing the nAChR cryo-EM and AChBP x-ray structures, Miyazawa et al. proposed that the ligand-binding domain can be approximately defined as two rigid domains, one the inner part, encompassing β1–β6 strands (residues 1–127), and the second the outer part, comprising β7–β10 strands (residues 142–205) (49). Upon agonist binding, the inner part rotates by $\sim$10° relative to the outer sheets during the gating process. Overall, the partition of the entire ligand-binding domain into two separate rigid bodies is in reasonable correspondence with a two-block TLS analysis. However, one major difference is evident between our analysis and the cryo-EM structures. In our simulation, the Cys-loop is not divided, but rather undergoes a concerted motion, contrary to the previous proposal of a rotation about an axis through the Cys-loop disulphide bridge (24). It is possible that the location of the Cys-loop toward the bottom of the extracellular domain may cause difficulty in modeling compared to other regions, which could affect our computational results. In fact, both concerted movement and lack of motion of the Cys-loop have been noted in previous MD simulations (7,21). Nevertheless, further investigations with more accurate models are needed to clarify this issue.

At a finer level of partitioning, the optimal TLS model gives rise to 14 blocks within a single α-subunit. In Fig. 4, we show the partitioned blocks, each of them colored differently. In the ligand-binding domain, two of the largest blocks are that shown in cyan (residues 73–156) and the red block formed by the β1 and β2 strands (residues 31–63). Each transmembrane helix is defined as a separate block; notable exceptions are M1 and M2, which make up a single block together with the connecting loop. Ten gating blocks have been identified so far by REFER analysis of the gating transition state (41): four in the extracellular domain (two in each α-subunit) and six in the transmembrane domains. The experiments also suggest that the entire M4 segment moves as a rigid body (41), whereas M2 is divided into two distinct blocks based upon different ϕ-values (50). The assignment of the entire M4 to a single block correlates fairly well with our TLS analysis. However, in contrast to the notion that M2 breaks in the middle of the helix at position 9′, no kink motion is seen in the M2 helix throughout the simulation; the entire M2 roughly moves as a rigid body. The β1–β2 and Cys-loops appear to form an important gating block experimentally (41), but do not belong to the same block according to our TLS analysis; the two loops move toward each other in a concerted motion, implying that their movements may occur at the same time along the gating pathway, giving rise to similar ϕ-values (51). The ligand-binding site comprises several loops that divide into separate gating blocks experimentally (18). However, the current

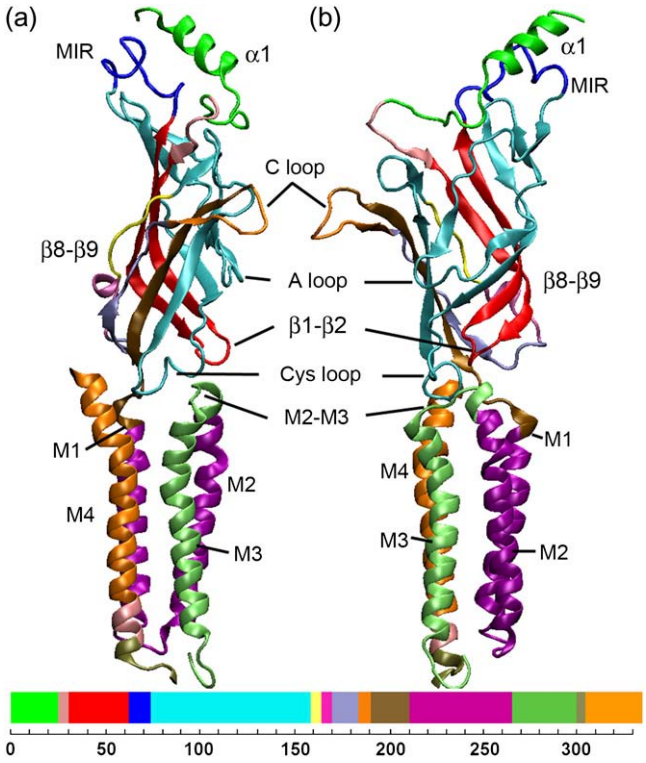

FIGURE 4 ''Block'' motion of the α7 receptor as suggested by the TLSMD analysis based on the simulation data. Fourteen blocks have been identified within a single α7 subunit, and are shown in different colors. The color bar on the bottom indicates the sequence information. (*a*) Front view, taken from the periphery of the receptor. (*b*) Rotated ~180° from the position in *a*.

TLSMD algorithm only considers contiguous runs of residues within the protein chain (48), and it is not possible to determine whether these loops correspond to the same or different blocks.

Coupling between Cys-loop and M2-M3 linker

A central question concerning the gating mechanism is how motions in the ligand-binding domain propagate to the ion pore, giving rise to substantial effort in probing the atomic details of this interdomain coupling (1,37,38). Even though our simulation time is evidently too short to reveal the full gating process, the current simulation provides some insights into the early events in gating, as well as the coupling between the ligand-binding and transmembrane domains. Our results so far suggest that movements of the two domains are strongly coupled, especially in subunits B and D, and that this dynamical coupling is possibly established through the interactions between the Cys-loop and the M2-M3 linker.

To further probe the structural bases of interdomain coupling, we generated cross-correlation plots from the MD simulation. As displayed in Fig. 5 *a*, extensive correlations are noted at the interface dividing the ligand-binding and transmembrane domains. If we draw horizontal stripes at the corresponding residues, 200–210 (β10-M1 linker) and 265–275 (M2-M3 linker), we see these stripes intersect yellow/orange spots corresponding to clusters of residues of interest. The 200–210 stripe intersects at residues 45–50 (β1-β2 linker), 130–142 (Cys-loop), 173–180 (β8-β9 loop), and 268–274 (M2-M3 linker). The 265–275 stripe intersects at residues 45–50 (β1-β2), 130–142 (Cys-loop), and 205–210 (β10-M1 linker). Some of these intersections correspond to interdomain pairs previously shown to form crucial links between binding and gating domains (12,24), and include the pairs M2-M3/β1-β2, M2-M3/β10-M1, and β10-M1/β1-β2 (Fig. 5 *a*, *circles*). Additional intersections correspond to potentially novel pairs of coupled domains, such as the M2-M3/Cys-loop, β10-M1/Cys-loop, and β10-M1/β8-β9 linker (Fig. 5 *a*, *squares*).

Correlated residues from the Cys-loop and the β10-M1 region are shown in an expanded view in Fig. 5 *b*; a similar correlation pattern is consistently seen in four out of five subunits. The primary region of correlation corresponds to a stretch of residues (138–146) from the Cys-loop/β7 strand and residues 198–205 in the β10-M1 region, indicating a concerted motion of these two strands. The second region reveals correlated motion between Val^{132} from the Cys-loop and Arg^{206} from the β10-M1 region. These two correlation patterns likely reflect the local fold of the protein, which couples the motion of the Cys-loop/β7 strand and β10-M1 region to the middle of the Cys-loop.

Correlated residues from the Cys-loop and the M2-M3 linker are shown in an expanded view in Fig. 5 *c*. The results reveal a cluster of hydrophobic residues involving Val^{132}-Phe^{135} from the Cys-loop and Pro^{269}-Ile^{271} from the M2-M3 linker; the pattern is seen in four out of five subunits. Closer inspection of the simulation trajectory reveals that the coupled motions may be mediated by stabilization of Phe^{135} in the hydrophobic crevice formed by Leu^{270} and Ile^{271}. Fig. 6 *a* plots the distance between the CZ atom of Phe^{135} and the C^{α} atom of Ile^{271} as a function of time; after ~4 ns, Phe^{135} moves closer to Ile^{271}. In the meantime, as shown in Fig. 6 *b*, the *z* axis position of M2 also decreases, indicating a downward shift of the M2 helix. Thus movement of the backbone of the Cys-loop leads to side-chain rotation of Phe^{135}, which then docks into the hydrophobic pocket made by the side chains of residues Leu^{270} and Ile^{271} from the apposing M2-M3 linker (Fig. 6, *c* and *d*). Through this newly formed contact, motion of the Cys loop is translated to the M2-M3 linker, which curls down and displaces M2 downward in the membrane. During the transition, the Phe^{135} side chain χ angle fluctuates back and forth for ~2 ns, but at 2.4 ns it flips from −160° to −60° (Fig. 6, *c* and *d*), remaining in this position for the rest of the simulation. More subtle changes are seen in the backbone angles.

A direct interaction between Phe^{135} and Leu^{270}/Ile^{271} is consistent with interpretations based on two chimera receptors

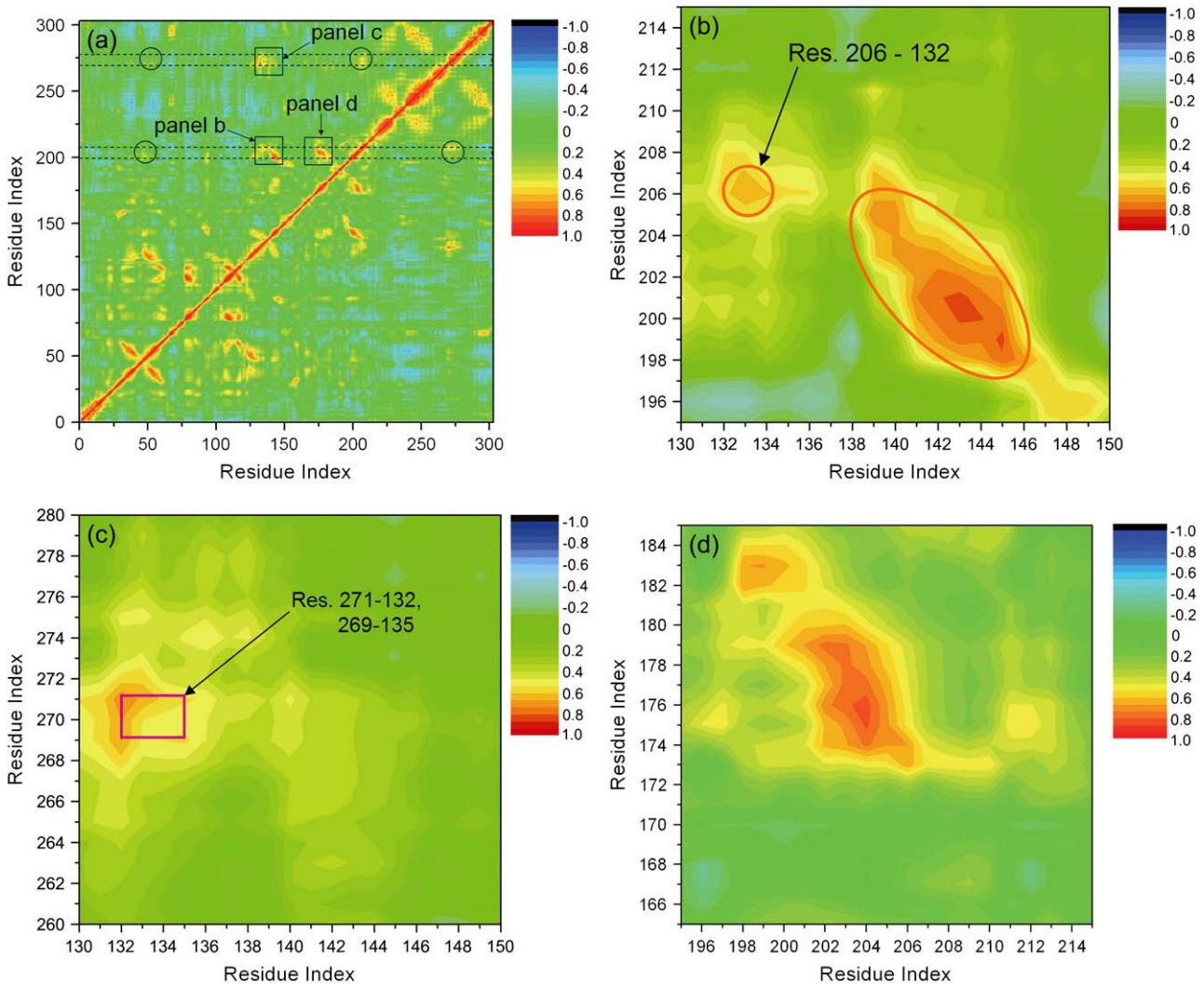

FIGURE 5 Correlated fluctuations of the C^{α} atoms in the α7 receptor, calculated from the MD simulation. The correlation maps are shown for correlated residues from (*a*) the A subunit, (*b*) the Cys-loop and the β10-M1 region, with the two primary regions of correlation highlighted by red circles, (*c*) the Cys-loop and the M2-M3 linker, with a coupled hydrophobic tetrad highlighted by a purple rectangular box, (*d*) the β10-M1 and the β8-β9 linker. The color bars on the right indicate the extent of the correlation. Residue pairs with a high level of correlated motions are shown in yellow, orange, and red. Anticorrelated motions are represented by the blue/cyan regions. Green indicates no correlation.

that structural matching of the Cys loop and M2-M3 residues is both essential and can fine-tune receptor function (14,52). Finally, Phe^{135}, Leu^{270}, and Ile^{271} are highly conserved among the nAChR family, suggesting that they contribute fundamentally in communicating motions between binding and pore domains. The proposed hydrophobic interaction of Phe^{135}, Leu^{270}, and Ile^{271} could be tested by measuring channel-gating kinetics after pairwise mutations of selected residues (12).

Dynamics of the transmembrane helices

Although insights into the complex dynamics of the transmembrane domain have emerged from MD simulations (53–56), it is still not clear how the ligand-binding domain affects pore dynamics, since most previous simulations used only the isolated transmembrane domain. A receptor model with both the ligand-binding and transmembrane domains was employed in the recent simulation by Law et al. (7), but in that model the transmembrane domain of the *Torpedo* receptor (24) was joined with a model of the ligand-binding domain based on the x-ray structure of AChBP (23), and solved by satisfying spatial restraints. The resulting model differed substantially from the current model, based on the 4-Å *Torpedo* receptor structure, particularly at the junction dividing binding and pore domains.

The time evolution of the minimum pore size and the corresponding *z* axis position is depicted in Fig. 7. During

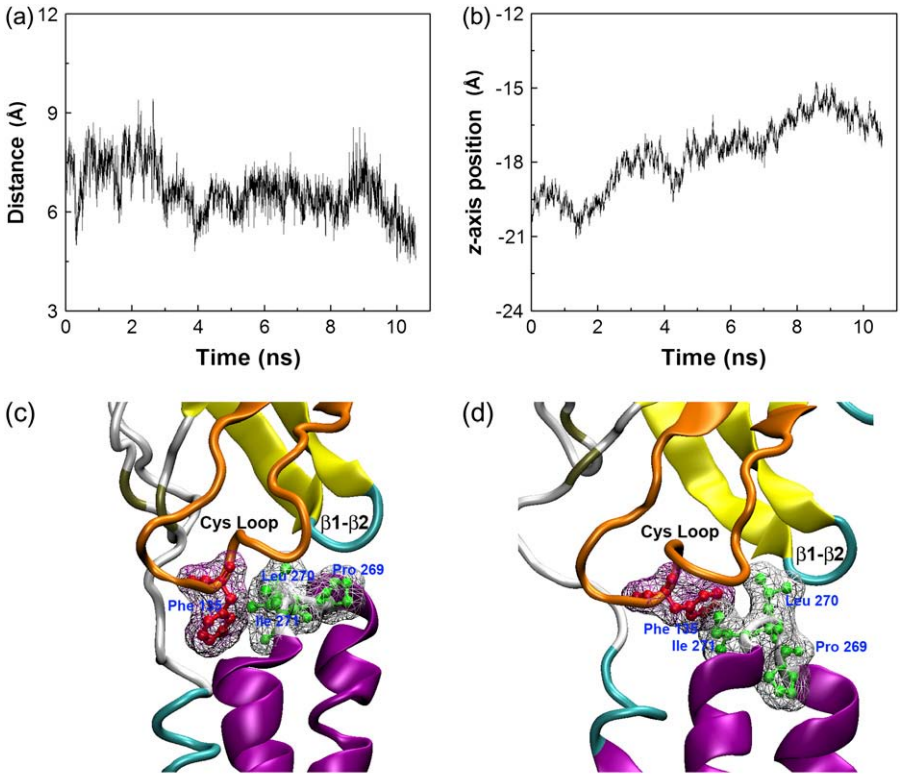

FIGURE 6 Correlated motion of Phe^{135} (located in the Cys-loop) and Ile^{271} (located in the M2-M3 linker) during the MD simulation. (*a*) Distance between Phe^{135} and Ile^{271} as a function of time. (*b*) Averaged *z* axis position of the M2 helix as a function of time. (*c* and *d*) Detailed views of the membrane interface region in the initial structure (*c*) and in a snapshot after 6 ns of MD simulation (*d*).

the simulation, the minimum pore size decreases slightly (from 2.8 to 2.2 Å), indicating a slight narrowing of the pore, in agreement with observations by Law et al. (7) and Corry (57). The position of the minimum pore radius begins near the intracellular end, near position 2′, shifts suddenly to position 9′, then to 13′, and gradually progresses to the upper part of the pore at position 20′.

Overall, the transmembrane helices are stable and retain their α-helical structures throughout the simulation (data not shown). Among the four transmembrane helices, M1 and M4 undergo less significant motions. The stability of M4 is consistent with the REFER (41) and photolabeling (58) experiments, but contrasts with observations in previous simulations. The significant motion of M4 in previous MD (7) and normal-mode (20) analyses has been attributed to the lack of the intervening vestibule domain and the lipid bilayer, respectively.

The downward movement of the M2-M3 linker is likely the cause of the significant structural changes of M2 and M3. Since M2 lines the inner wall of the channel, we focus our analysis on its conformational changes. Several likely motions have been suggested for the M2 helices during gating, such as a rigid-body rotation (7,24), a kink occurring in the middle of the pore (24,54), or a tilting motion that opens the intracellular end (17). However, the fundamental motion of M2 that opens the pore is still largely unknown. Using a rigid-body fitting procedure, we monitored the rotation, kink, and tilting motions of the five M2 helices during the simulation. First, neither a kinking nor a rotation about the channel axis is evident in the simulation. The previous MD simulation also concluded that M2 does not kink (7).

Our analyses reveal large fluctuations of both lateral and radial tilting angles for M2 (Fig. 8). Concerted lateral tilting of all five M2 helices would increase the pore size at every position along the pore axis, except at the hinge point, whereas simultaneous radial tilting would make one end wider but the other end narrower. It is also worth noting that a concerted lateral tilting that occurs in the same direction is essentially similar to a rotation of M2 about an axis passing through the M2-M3 linker. The lateral tilting angle tends to decrease for all five M2 helices, as compared to the initial configuration (Fig. 8 *c*), which partially accounts for the shrinkage of the pore size during the simulation (Fig. 7 *a*). The radial tilting angle shows asymmetrical changes for the five M2 helices, increasing substantially in subunits B and D, fluctuating in subunit C, but changing little in subunits A and E (Fig. 8 *d*). The asymmetrical radial tilting of the five M2 helices leads to a slightly elongated channel pore. More important, the radial tilting of M2 opens up the intracellular end while it narrows the extracellular end, which explains the shift in the minimum pore position in Fig. 7 *b*. Based on the observation that the minimum position moves from position 9′ to 16′/20′ (Fig. 7 *b*), the pivot point for radial tilting

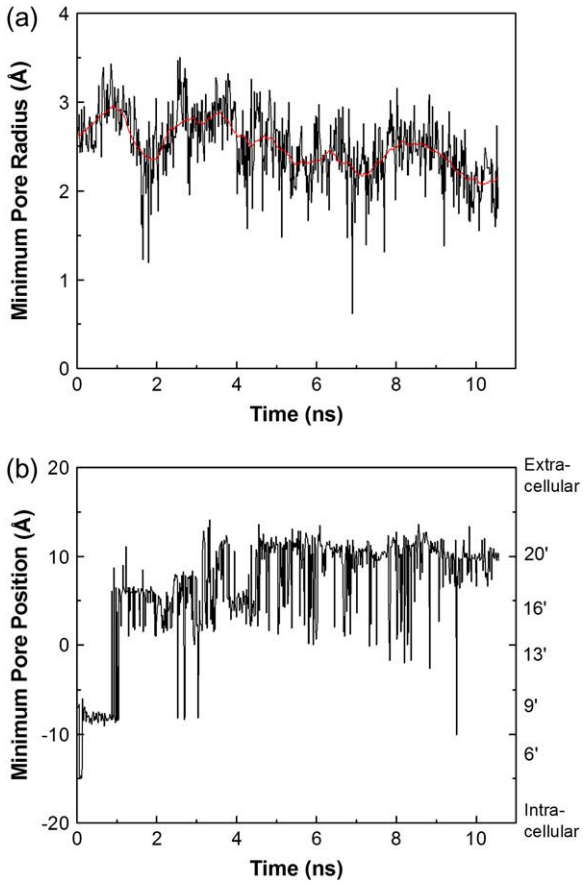

FIGURE 7 (*a*) Minimum pore radius and (*b*) *z* axis position of the minimum pore radius as a function of time during the MD simulation (with the conventional numbering for M2 residues depicted on the right axis). The center of the pore domain is set to zero, with positive *z* values toward the extracellular end.

occurs around position 13′. The observed tilting motion is in accord with the recent studies of a Cys-loop receptor chimera (17). However, the location of the pivot point disagrees with that experimental result, and also with the previous conclusion that leucines at position 9′ become closer in the open state (59). Our results suggest that structural alteration of the Val at position 13′ in M2 may alter rigid body movement of M2 and thus alter channel gating.

The simulation also reveals penetration of water molecules throughout the pore (Fig. 9), in line with previous simulations (54,57) and also consistent with potential-of-mean-force calculations, indicating that the barrier height for passage of a water molecule is only $\sim 2\ k_BT$ (60). However, close inspection of the simulation trajectory reveals that toward the beginning of the simulation, the middle of the pore (positions 9′ and 13′) is dehydrated, whereas the intracellular end is filled with water molecules due to tilting of M2. As the simulation progresses, two of the M2 helices are pushed downward, collapsing the hydrophobic gate and allowing the side chains of $Leu^{9'}$ and $Val^{13'}$ to move sideways, thus permitting water to come through. This observation agrees with the idea of a hydrophobic gate, proposed previously (24). A detailed view of the two hydrophobic rings is displayed in Fig. 10. In the initial configuration, the pore is symmetrically oriented to form a hydrophobic barrier for ions, and even for water (Fig. 10 *a*). After 6 ns of simulation, the hydrophobic residues orient more asymmetrically, which facilitates full hydration of the pore (Fig. 10 *b*).

DISCUSSION

Exploring the transition pathways between functional states of the nAChR is a challenging problem for both experiment and computation. Aspects of this system that present special difficulties for computation are the limited resolution of the available cryo-EM structure (36), the lack of structural data for the open state, and the broad and complex nature of the transition-state ensemble, which may involve multiple microstates (47). Another complication arises from the vast range of timescales that characterize the gating process, most of which lie outside the nanosecond scope of contemporary molecular-dynamics simulations (61). Thus, the implications for the gating mechanism drawn from this study necessarily involve an element of extrapolation. In this respect, it is worth noting that the gating motion has been envisioned as having a low-frequency, quasiharmonic nature (42,62). Therefore, an analysis of the global collective motions of the system via quasiharmonic or PCA analysis may provide a reasonable way to extrapolate the simulation data from a relatively short MD trajectory to render motions occurring on a longer timescale.

In this study, we used MD simulation to explore the global conformational dynamics of the human α7 nAChR. Our PCA analysis indicates that the α7 receptor model is highly elastic, as revealed by the very cooperative global motions involving many atoms. The observed large-scale motions are likely an intrinsic property of the architecture of α7. That is, these motions are not driven by the binding of agonist, as the simulation is performed in the absence of ligand, nor do they depend on the subtle details of the structure. The binding of the ligand possibly just perturbs the preexisting equilibrium among two or more possible states, thereby mediating channel activity. Moreover, there is increasing evidence to suggest that concerted motions at low frequency may be associated with channel gating (62,63). Two recent normal-mode analysis studies proposed, as the gating mechanism, a quaternary twisting motion in which symmetrical rotations of the five M2 segments around a longitudinal axis relieve the hydrophobic hindrance, leading to an open channel (19,20). Although this mechanism finds support from a body of experimental data, some experimental results still cannot be properly accounted for. In particular, the rotational movements of the pore-lining helices have been disfavored by substituted-cysteine-accessibility experiments (64,65) and proton block of single-channel currents (16). In our lowest-frequency PCA

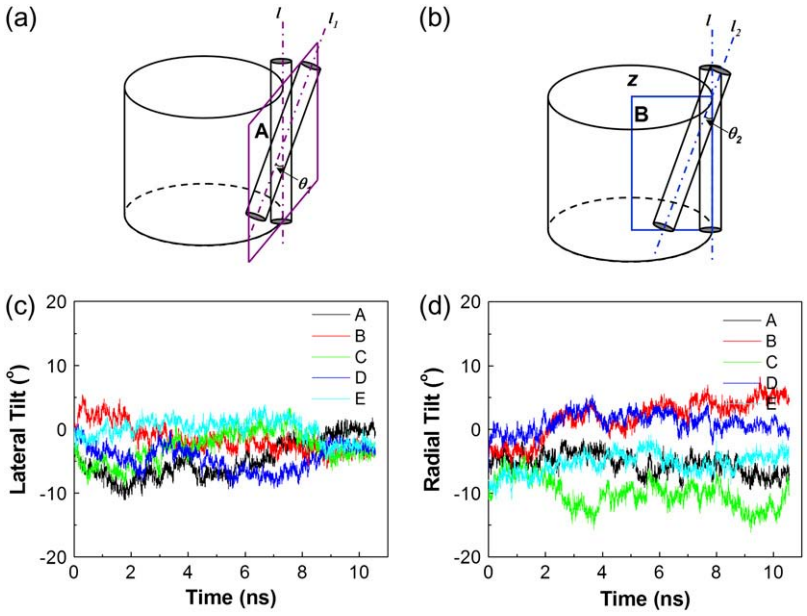

FIGURE 8 (*a* and *b*) Schematic representations of lateral tilting θ_1 and radial tilting θ_2. See Methods section for the definitions of these two angles. (*c*) Lateral tilting and (*d*) radial tilting motions of the five M2 helices as a function of time during the MD simulation.

mode of motion, movements of the ligand-binding domain (C-loop and α1 helix) are highly correlated with those of the M2 and M3 helices. Our simulation also reveals that the downward movement of the M2-M3 linker results in a downward shift of two M2 helices and tilting motions of all five M2 helices. This suggests that conformational changes within the extracellular and transmembrane domains may be communicated through the M2-M3 linker, and that a tilting motion of M2 may play a role in channel gating.

Despite the limitation of the current TLSMD algorithm that can identify segmental blocks along a contiguous chain, useful insights emerge for comparison with experimental data. In contrast to two blocks in the extracellular domain found experimentally (47), the six-block partition produces the best fit to our atomic displacement parameters. The difference in block partitioning compared to experiments is not surprising, because the criteria for defining the block partitions are clearly different. The REFER experiment uses ϕ-values to identify blocks (51), whereas the TLS analysis uses anisotropic atomic displacement parameters along

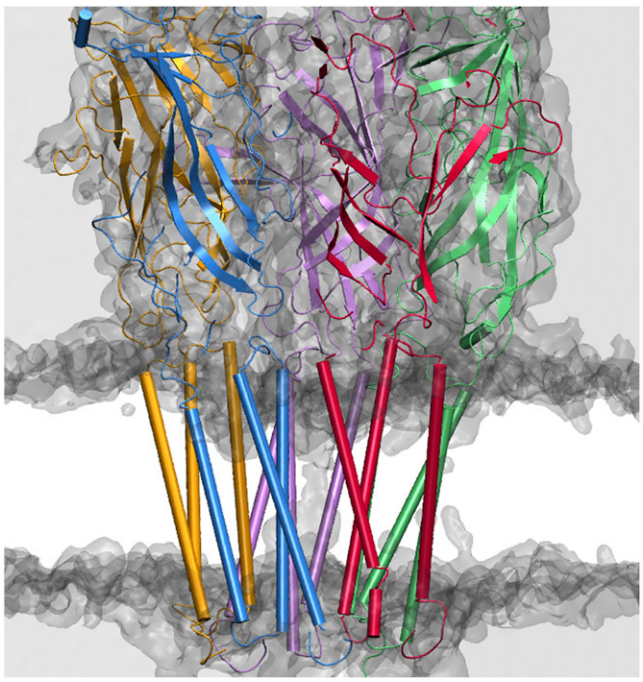

FIGURE 9 Isosurfaces of time-averaged water density during the simulation. The surface corresponds to the isodensity contour, ~0.4 of the bulk water density. The receptor structure is shown in cartoon representation, with each subunit colored differently.

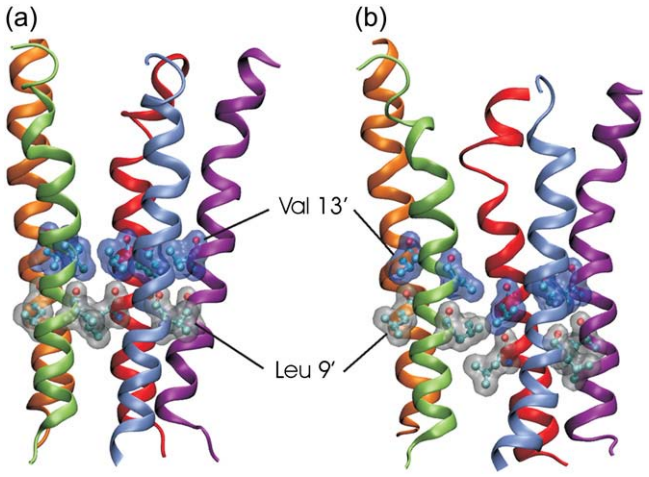

FIGURE 10 Detailed view of two hydrophobic residues, Leu$^{9'}$ (248) and Val$^{13'}$ (252), (*a*) in the initial structure, and (*b*) in a snapshot after 10 ns of MD simulation.

consecutive segments of the protein chain (48). Moreover, our 10-ns simulation likely only samples the local conformational space from the presumed closed state, whereas the observed dynamics may represent part of the gating motion due to the elasticity of the protein.

Overall, a fully water-filled pore is observed in the simulation. However, toward the beginning of the simulation, the pore is only partially hydrated for ~1–2 ns. Consistent with previous observations, the dry region is not the narrowest, but actually the most hydrophobic one (9′ and 13′ positions). The dry region starts to be occupied with water molecules when the side chains of $Leu^{9'}$ and $Val^{13'}$ move sideways in response to downward motions of two M2 helices. Whereas no significant kinking of M2 occurs, tilting of M2 is observed within 10 ns of the simulation. The concerted tilting of all five M2 helices widens the intracellular end of the pore, suggesting that tilting of M2 may be involved in early stages of channel dynamics, leading to gating. Another striking observation is a hydrophobic coupling between the Cys-loop (Phe^{135}) and the M2-M3 linker (Leu^{270}/Ile^{271}), which acts as a pivot point linking the structural rearrangements in the ligand-binding domain to the motion of the transmembrane domain.

Finally, the ligand-binding domain greatly impacts the dynamics of the transmembrane helices. The ligand-binding domain not only initiates the motion that is translated to the pore domain, but also provides an important environment for several connecting loops located at the interface dividing binding and pore domains. Previous simulations of the transmembrane helices showed partial unfolding of the two helical ends of the transmembrane segments (53,56), which could lead to unrealistic movements of the transmembrane domains, especially the M2 and M3 helices.

CONCLUSION

In summary, consistent global motion of the α7 acetylcholine receptor is observed from various analyses of a 10-ns MD simulation. The low-frequency global motion involves a bending motion hinged at the β10-M1 region, accompanied by tilting motions of the five M2 helices. Outward movements of the C-loop—which, it has been proposed, acts as a handle of a lever—correlate strongly with the tilting motions of the transmembrane helices. The observed motion provides a possible model of dynamical coupling that may indicate the start of the gating step. Our simulation results suggest several experimental tests of our inferences. First, the interaction between Phe^{135} in the Cys-loop and Leu^{270}/Ile^{271} in the M2-M3 linker, identified computationally, could be tested using natural and unnatural amino acid substitution. Second, mutating $Val^{13'}$ residues might impair M2 tilting and alter channel gating. Third, it is predicted that M1 and M2 move together and thus should have similar ϕ-values. Future studies of the α7 receptor will benefit from a close interplay between experimental approaches and simulation, and likely require a more detailed structural understanding of the channel in the closed and open states.

SUPPLEMENTARY MATERIAL

To view all of the supplemental files associated with this article, visit www.biophysj.org.

We thank Richard Law for providing us with the original RMSF data presented in Fig. 2 *a*.

I.I. acknowledges financial support from the Burroughs Wellcome Fund in the form of a La Jolla Interfaces in Science fellowship. Support to J.A.M. for this project was provided partly by the National Science Foundation (NSF), National Institutes of Health, San Diego Supercomputer Center, Howard Hughes Medical Institute, National Biomedical Computation Resource, and NSF Center for Theoretical Biological Physics.

REFERENCES

1. Sine, S. M., and A. G. Engel. 2006. Recent advances in Cys-loop receptor structure and function. *Nature*. 440:448–455.
2. Celie, P. H., S. E. van Rossum-Fikkert, W. J. van Dijk, K. Brejc, A. B. Smit, and T. K. Sixma. 2004. Nicotine and carbamylcholine binding to nicotinic acetylcholine receptors as studied in AChBP crystal structures. *Neuron*. 41:907–914.
3. Hansen, S. B., G. Sulzenbacher, T. Huxford, P. Marchot, P. Taylor, and Y. Bourne. 2005. Structures of *Aplysia* AChBP complexes with nicotinic agonists and antagonists reveal distinctive binding interfaces and conformations. *EMBO J*. 24:3635–3646.
4. Gao, F., N. Bren, T. P. Burghardt, S. Hansen, R. H. Henchman, P. Taylor, J. A. McCammon, and S. M. Sine. 2005. Agonist-mediated conformational changes in acetylcholine-binding protein revealed by simulation and intrinsic tryptophan fluorescence. *J. Biol. Chem.* 280:8443–8451.
5. Shi, J., J. R. Koeppe, E. A. Komives, and P. Taylor. 2006. Ligand-induced conformational changes in the acetylcholine-binding protein analyzed by hydrogen-deuterium exchange mass spectrometry. *J. Biol. Chem.* 281:12170–12177.
6. Gao, F., G. Mer, M. Tonelli, S. B. Hansen, T. P. Burghardt, P. Taylor, and S. M. Sine. 2006. Solution NMR of acetylcholine binding protein reveals agonist-mediated conformational change of the C-loop. *Mol. Pharmacol*. 70:1230–1235.
7. Law, R. J., R. H. Henchman, and J. A. McCammon. 2005. A gating mechanism proposed from a simulation of a human α7 nicotinic acetylcholine receptor. *Proc. Natl. Acad. Sci. USA*. 102:6813–6818.
8. Karlin, A., and M. H. Akabas. 1998. Substituted-cysteine accessibility method. *Methods Enzymol*. 293:123–145.
9. Bera, A. K., M. Chatav, and M. H. Akabas. 2002. GABA(A) receptor M2-M3 loop secondary structure and changes in accessibility during channel gating. *J. Biol. Chem*. 277:43002–43010.
10. Horenstein, J., D. A. Wagner, C. Czajkowski, and M. H. Akabas. 2001. Protein mobility and GABA-induced conformational changes in GABA(A) receptor pore-lining M2 segment. *Nat. Neurosci*. 4:477–485.
11. Kash, T. L., A. Jenkins, J. C. Kelley, J. R. Trudell, and N. L. Harrison. 2003. Coupling of agonist binding to channel gating in the GABA(A) receptor. *Nature*. 421:272–275.
12. Lee, W. Y., and S. M. Sine. 2005. Principal pathway coupling agonist binding to channel gating in nicotinic receptors. *Nature*. 438:243–247.
13. Cheng, X., H. Wang, B. Grant, S. M. Sine, and J. A. McCammon. 2006. Targeted molecular dynamics study of C-loop closure and channel gating in nicotinic receptors. *PLoS Comput. Biol*. 2:e134.

14. Bouzat, C., F. Gumilar, G. Spitzmaul, H. L. Wang, D. Rayes, S. B. Hansen, P. Taylor, and S. M. Sine. 2004. Coupling of agonist binding to channel gating in an ACh-binding protein linked to an ion channel. *Nature*. 430:896–900.
15. Unwin, N. 1995. Acetylcholine receptor channel imaged in the open state. *Nature*. 373:37–43.
16. Cymes, G. D., Y. Ni, and C. Grosman. 2005. Probing ion-channel pores one proton at a time. *Nature*. 438:975–980.
17. Paas, Y., G. Gibor, R. Grailhe, N. Savatier-Duclert, V. Dufresne, M. Sunesen, L. P. de Carvalho, J. P. Changeux, and B. Attali. 2005. Pore conformations and gating mechanism of a Cys-loop receptor. *Proc. Natl. Acad. Sci. USA*. 102:15877–15882.
18. Grosman, C., M. Zhou, and A. Auerbach. 2000. Mapping the conformational wave of acetylcholine receptor channel gating. *Nature*. 403:773–776.
19. Taly, A., M. Delarue, T. Grutter, M. Nilges, N. Le Novere, P. J. Corringer, and J. P. Changeux. 2005. Normal mode analysis suggests a quaternary twist model for the nicotinic receptor gating mechanism. *Biophys. J.* 88:3954–3965.
20. Cheng, X., B. Lu, B. Grant, R. J. Law, and J. A. McCammon. 2006. Channel opening motion of α7 nicotinic acetylcholine receptor as suggested by normal mode analysis. *J. Mol. Biol.* 355:310–324.
21. Henchman, R. H., H. L. Wang, S. M. Sine, P. Taylor, and J. A. McCammon. 2003. Asymmetric structural motions of the homomeric α7 nicotinic receptor ligand binding domain revealed by molecular dynamics simulation. *Biophys. J.* 85:3007–3018.
22. Henchman, R. H., H. L. Wang, S. M. Sine, P. Taylor, and J. A. McCammon. 2005. Ligand-induced conformational change in the α7 nicotinic receptor ligand binding domain. *Biophys. J.* 88:2564–2576.
23. Brejc, K., W. J. van Dijk, R. V. Klaassen, M. Schuurmans, J. van Der Oost, A. B. Smit, and T. K. Sixma. 2001. Crystal structure of an ACh-binding protein reveals the ligand-binding domain of nicotinic receptors. *Nature*. 411:269–276.
24. Miyazawa, A., Y. Fujiyoshi, and N. Unwin. 2003. Structure and gating mechanism of the acetylcholine receptor pore. *Nature*. 423:949–955.
25. Sali, A., and T. L. Blundell. 1993. Comparative protein modelling by satisfaction of spatial restraints. *J. Mol. Biol.* 234:779–815.
26. Sali, A., L. Potterton, F. Yuan, H. van Vlijmen, and M. Karplus. 1995. Evaluation of comparative protein modeling by MODELLER. *Proteins*. 23:318–326.
27. Laskowski, R. A., M. W. MacArthur, D. S. Moss, and J. M. Thornton. 1993. PROCHECK: a program to check the stereochemical quality of protein structures. *J. Appl. Crystallogr.* 26:283–291.
28. Sippl, M. J. 1993. Recognition of errors in three-dimensional structures of proteins. *Protein*. 17:355–362.
29. Phillips, J. C., R. Braun, W. Wang, J. Gumbart, E. Tajkhorshid, E. Villa, C. Chipot, R. D. Skeel, L. Kale, and K. Schulten. 2005. Scalable molecular dynamics with NAMD. *J. Comput. Chem.* 26:1781–1802.
30. MacKerrell, A. D., D. Bashford, M. Bellott, R. L. Dunbrack, J. D. Evanseck, M. J. Field, S. Fischer, J. Gao, H. Guo, S. Ha, D. Joseph-McCarthy, L. Kuchnir, K. Kuczera, F. T. K. Lau, C. Mattos, S. Michnick, T. Ngo, D. T. Nguyen, B. Prodhom, W. E. Reiher III, B. Roux, M. Schlenkrich, J. C. Smith, R. Stote, J. Straub, M. Watanabe, M. Watanabe, D. Yin, and M. Karplus. 1998. All-atom empirical potential for molecular modeling and dynamics studies of proteins. *J. Phys. Chem. B*. 102:3586–3616.
31. Darden, T., D. York, and L. Pedersen. 1993. Particle mesh Ewald: An N log (N) method for Ewald sums in large systems. *J. Chem. Phys.* 98:10089–10092.
32. Van Der Spoel, D., E. Lindahl, B. Hess, G. Groenhof, A. E. Mark, and H. J. Berendsen. 2005. GROMACS: fast, flexible, and free. *J. Comput. Chem.* 26:1701–1718.
33. Painter, J., and E. A. Merritt. 2006. TLSMD web server for the generation of multi-group TLS models. *J. Appl. Crystallogr.* 39:109–111.
34. Smart, O. S., J. G. Neduvelil, X. Wang, B. A. Wallace, and M. S. Sansom. 1996. HOLE: a program for the analysis of the pore dimensions of ion channel structural models. *J. Mol. Graph.* 14:354–360.
35. Humphrey, W., A. Dalke, and K. Schulten. 1996. VMD: visual molecular dynamics. *J. Mol. Graph. Model.* 14:33–38.
36. Unwin, N. 2005. Refined structure of the nicotinic acetylcholine receptor at 4A resolution. *J. Mol. Biol.* 346:967–989.
37. Lester, H. A., M. I. Dibas, D. S. Dahan, J. F. Leite, and D. A. Dougherty. 2004. Cys-loop receptors: new twists and turns. *Trends Neurosci.* 27:329–336.
38. Absalom, N. L., T. M. Lewis, and P. R. Schofield. 2004. Mechanisms of channel gating of the ligand-gated ion channel superfamily inferred from protein structure. *Exp. Physiol.* 89:145–153.
39. Dahan, D. S., M. I. Dibas, E. J. Petersson, V. C. Auyeung, B. Chanda, F. Bezanilla, D. A. Dougherty, and H. A. Lester. 2004. A fluorophore attached to nicotinic acetylcholine receptor β M2 detects productive binding of agonist to the $\alpha\delta$ site. *Proc. Natl. Acad. Sci. USA*. 101:10195–10200.
40. Wick, M. J., S. J. Mihic, S. Ueno, M. P. Mascia, J. R. Trudell, S. J. Brozowski, Q. Ye, N. L. Harrison, and R. A. Harris. 1998. Mutations of gamma-aminobutyric acid and glycine receptors change alcohol cutoff: evidence for an alcohol receptor? *Proc. Natl. Acad. Sci. USA*. 95:6504–6509.
41. Mitra, A., T. D. Bailey, and A. L. Auerbach. 2004. Structural dynamics of the M4 transmembrane segment during acetylcholine receptor gating. *Structure*. 12:1909–1918.
42. Miyashita, O., J. N. Onuchic, and P. G. Wolynes. 2003. Nonlinear elasticity, proteinquakes, and the energy landscapes of functional transitions in proteins. *Proc. Natl. Acad. Sci. USA*. 100:12570–12575.
43. Galzi, J. L., D. Bertrand, A. Devillers-Thiery, F. Revah, S. Bertrand, and J. P. Changeux. 1991. Functional significance of aromatic amino acids from three peptide loops of the α7 neuronal nicotinic receptor site investigated by site-directed mutagenesis. *FEBS Lett.* 294:198–202.
44. Corringer, P. J., N. Le Novere, and J. P. Changeux. 2000. Nicotinic receptors at the amino acid level. *Annu. Rev. Pharmacol. Toxicol.* 40:431–458.
45. Mukhtasimova, N., C. Free, and S. M. Sine. 2005. Initial coupling of binding to gating mediated by conserved residues in the muscle nicotinic receptor. *J. Gen. Physiol.* 126:23–39.
46. Campos-Caro, A., S. Sala, J. J. Ballesta, F. Vicente-Agullo, M. Criado, and F. Sala. 1996. A single residue in the M2-M3 loop is a major determinant of coupling between binding and gating in neuronal nicotinic receptors. *Proc. Natl. Acad. Sci. USA*. 93:6118–6123.
47. Auerbach, A. 2005. Gating of acetylcholine receptor channels: brownian motion across a broad transition state. *Proc. Natl. Acad. Sci. USA*. 102:1408–1412.
48. Painter, J., and E. A. Merritt. 2006. Optimal description of a protein structure in terms of multiple groups undergoing TLS motion. *Acta Crystallogr. D*. 62:439–450.
49. Unwin, N., A. Miyazawa, J. Li, and Y. Fujiyoshi. 2002. Activation of the nicotinic acetylcholine receptor involves a switch in conformation of the α subunits. *J. Mol. Biol.* 319:1165–1176.
50. Cymes, G. D., C. Grosman, and A. Auerbach. 2002. Structure of the transition state of gating in the acetylcholine receptor channel pore: a ϕ-value analysis. *Biochemistry*. 41:5548–5555.
51. Zhou, Y., J. E. Pearson, and A. Auerbach. 2005. ϕ-value analysis of a linear, sequential reaction mechanism: theory and application to ion channel gating. *Biophys. J.* 89:3680–3685.
52. Grutter, T., L. P. de Carvalho, V. Dufresne, A. Taly, S. J. Edelstein, and J. P. Changeux. 2005. Molecular tuning of fast gating in pentameric ligand-gated ion channels. *Proc. Natl. Acad. Sci. USA*. 102:18207–18212.
53. Xu, Y., F. J. Barrantes, X. Luo, K. Chen, J. Shen, and H. Jiang. 2005. Conformational dynamics of the nicotinic acetylcholine receptor channel: a 35-ns molecular dynamics simulation study. *J. Am. Chem. Soc.* 127:1291–1299.
54. Hung, A., K. Tai, and M. S. Sansom. 2005. Molecular dynamics simulation of the M2 helices within the nicotinic acetylcholine receptor transmembrane domain: structure and collective motions. *Biophys. J.* 88:3321–3333.

55. Saladino, A. C., Y. Xu, and P. Tang. 2005. Homology modeling and molecular dynamics simulations of transmembrane domain structure of human neuronal nicotinic acetylcholine receptor. *Biophys. J.* 88:1009–1017.

56. Saiz, L., and M. L. Klein. 2005. The transmembrane domain of the acetylcholine receptor: insights from simulations on synthetic peptide models. *Biophys. J.* 88:959–970.

57. Corry, B. 2006. An energy-efficient gating mechanism in the acetylcholine receptor channel suggested by molecular and Brownian dynamics. *Biophys. J.* 90:799–810.

58. Leite, J. F., M. P. Blanton, M. Shahgholi, D. A. Dougherty, and H. A. Lester. 2003. Conformation-dependent hydrophobic photolabeling of the nicotinic receptor: electrophysiology-coordinated photochemistry and mass spectrometry. *Proc. Natl. Acad. Sci. USA.* 100:13054–13059.

59. Kearney, P. C., H. Zhang, W. Zhong, D. A. Dougherty, and H. A. Lester. 1996. Determinants of nicotinic receptor gating in natural and unnatural side chain structures at the M2 9′ position. *Neuron.* 17:1221–1229.

60. Beckstein, O., and M. S. Sansom. 2006. A hydrophobic gate in an ion channel: the closed state of the nicotinic acetylcholine receptor. *Phys. Biol.* 3:147–159.

61. Chakrapani, S., and A. Auerbach. 2005. A speed limit for conformational change of an allosteric membrane protein. *Proc. Natl. Acad. Sci. USA.* 102:87–92.

62. Valadie, H., J. J. Lacapcre, Y. H. Sanejouand, and C. Etchebest. 2003. Dynamical properties of the MscL of *Escherichia coli*: a normal mode analysis. *J. Mol. Biol.* 332:657–674.

63. Shen, Y., Y. Kong, and J. Ma. 2002. Intrinsic flexibility and gating mechanism of the potassium channel KcsA. *Proc. Natl. Acad. Sci. USA.* 99:1949–1953.

64. Wilson, G. G., and A. Karlin. 1998. The location of the gate in the acetylcholine receptor channel. *Neuron.* 20:1269–1281.

65. Wilson, G. G., and A. Karlin. 2001. Acetylcholine receptor channel structure in the resting, open, and desensitized states probed with the substituted-cysteine-accessibility method. *Proc. Natl. Acad. Sci. USA.* 98:1241–1248.